This article has been accepted for publication in IEEE Transactions on Industry Applications. This is the author's version which has not been fully edited and content may change prior to final publication. Citation information: DOI 10.1109/TIA.2023.3336312

A Combined Design Procedure of High-Speed/High-Power PMSMs for an Adiabatic Compressed Air Energy Storage System

Andrea Floris, *Member, IEEE*, Alfonso Damiano, *Senior Member, IEEE*, Alessandro Serpi, *Member, IEEE*

***Abstract* — This paper presents a Combined Design Procedure (CDP) applied to modular high-speed/high-power Permanent Magnet Synchronous Machines (PMSMs) for an Adiabatic Compressed Air Energy Storage system (ACAES). Particularly, the modular structure enables higher maximum speed and flexibility compared to a monolithic PMSM as a suitable number of identical mechanically series-connected modules can be employed. These share the same speed and contribute together to the high overall power required by ACAES, thus avoiding excessive volume requirements and low-speed operation. The modular PMSM design has been accomplished by the proposed CDP, which exhibits multi-physic and optimization features thanks to both analytical and Finite Element Analysis (FEA) approaches. The former enables a rapid preliminary design that satisfies a given objective function, by complying with all electromagnetic and mechanical constraints. Such a preliminary design is then refined by the FEA approach, which accounts also for thermal constraints, and guarantees a better cost function optimization through a genetic algorithm. In this regard, different objective functions have been considered, leading to different PMSM configurations. The corresponding performance analysis reveals that all PMSM configurations comply with electromagnetic, mechanical, and thermal constraints, by guaranteeing design specifications as well.**

***Index Terms* — Adiabatic compressed air energy storage system, Combined design procedure, Finite element analysis, Genetic algorithms, Modular systems, Optimization.**

I. INTRODUCTION

In the last decade, the increase of Renewable Energy Sources (RESs) has posed significant challenges for the electricity industry, switching the electrical system from a hierarchical and highly-programmable framework to a distributed, more sustainable but less predictable one [1], [2]. This change has entailed the need to develop increasingly efficient Energy Storage Systems (ESSs), which are able to act not only as generators or loads, but also as providers of ancillary services [3].

Among the different ESS technology proposed for high power and energy storage applications (1-10 MW, tens of MWh), Compressed Air Energy Storage systems (CAESs) represent a viable solution due to the higher energy density, relatively lower costs, higher efficiency, and better technological maturity than other ESSs [4]. Furthermore, CAES is particularly attractive thanks to the possibility of repurposing disused mining cavities as a reservoir for compressed air [5]. Adiabatic CAES (ACAES) represents the most promising solution among the different CAES configurations due to the high efficiency, relatively low costs, and enhanced flexibility [6]–[8]. ACAES mainly consists of a series of Turbomachines (TMs, compressors and turbines), a tank to store the compressed air, and a thermal ESS. Each TM is coupled to one or more electrical machines, which can operate as either motor or generator according to the specific task. Recent CAES technology is pushing towards the use of high-speed electrical machines, which enable several potential advantages, e.g. weight reduction and overall system efficiency increase compared to low-speed counterparts. Particularly, given the very high-speed operation of TMs, the employment of high-speed electrical machines would ensure no or reduced gear ratio, thus removing, or at least simplifying, the transmission system with an overall efficiency increase [9].

Rotor-wounded synchronous or induction machines are generally used for CAES; the former are characterized by high power density and efficiency, but the use of a double winding makes them more likely to fail, and increases maintenance needs. On the other hand, induction machines exhibit robust rotor structure and low maintenance requirements, but at the cost of lower efficiency due to increased rotor losses. A valid alternative to both is represented by Permanent Magnet Synchronous Machines (PMSMs) due to their very high power and torque densities, high efficiency and high-speed operation, especially as far as advanced PMSM design and control strategies are concerned [10], [11]. However, the design of high-power/speed PMSM presents several critical issues related to electromagnetic, mechanical, and thermal aspects, which should be addressed accurately and synergically [12].

In this context, the design and optimization of a high-power/speed surface-mounted PMSM suitable for 9.9 MW ACAES is presented in [13]. In particular, a modular configuration has been proposed, namely multiple PMSM modules are mechanically series-connected to each other, sharing the same output shaft and speed. This configuration, barely reported in the literature as modular cascade machine and for automotive applications only [14], [15], is proposed for high-power stationary applications in this work. This is due to its very promising advantages, such as high fault-tolerant capability, highly-integrated design, optimal power sizing and

Andrea Floris, Alfonso Damiano and Alessandro Serpi are with the Department of Electrical and Electronic Engineering of the University of Cagliari, Italy (andrea.floris86@unica.it)

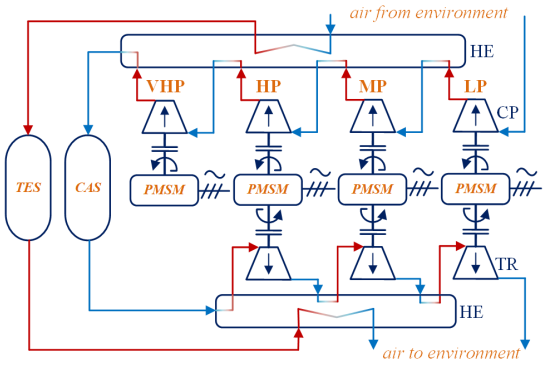

Fig. 1. An overview of the ACAES considered in this paper.

TABLE I. ACAES MAIN PARAMETERS

Description	Unit	Value
Rated charging power	*MW*	*6.8*
Rated discharging power	*MW*	*9.9*
Stored energy	*MWh*	*39.0*
Deliverable energy	*MWh*	*27.9*
Charging time	*h*	*6*
Discharging time	*h*	*3*

TABLE II. TURBOMACHINE MAIN PARAMETERS

	Stage	TM	Power [MW]	Speed [krpm]
Compressors	*Low pressure*	CP-LP	*1.9*	*12.7*
	Medium pressure	CP-MP	*1.7*	*21.8*
	High pressure	CP-HP	*1.7*	*28.6*
	Very high pressure	CP-VHP	*1.5*	*29.3*
	Overall	-	*6.8*	-
Turbines	*Low pressure*	TR-LP	*3.3*	*7.3*
	Medium pressure	TR-MP	*3.3*	*16.7*
	High pressure	TR-HP	*3.3*	*30*
	Overall	-	*9.9*	-

split by varying the number and control targets of single modules, thus reducing designing, manufacturing, and maintenance costs [14], [15]. A modular configuration also enables high-speed operation because the reduced size compared to monolithic solutions mitigate the mechanical stress, by increasing efficiency and flexibility as well [13].

The PMSM proposed in [13] has been design by an analytical approach, which starts from well-defined design targets, e.g. rated power/torque/speed, based on which the main PMSM parameters are derived through several design equations, which accounts for electromagnetic and mechanical targets and constraints. This analytical approach is quite fast but design results could be overly rough as the employment of excessively accurate modeling is not advisable. This is because an advanced multi-physic knowledge would be required and, even so, the analytical method would become too complex and, thus, slow to implement. Much more accurate design results can be achieved through FEA approaches, which easily include multi-physic targets and constraints. However, high computational efforts are required, as well as a rough idea of the numeric range of the main machine parameters.

Consequently, starting from the preliminary analytical PMSM design reported in [13], a more accurate design is presented in this paper, which consists of a multi-physic Combined Design Procedure (CDP) based on both analytical and Finite Element Analysis (FEA) approaches. The CDP integrates electromagnetic, mechanical, and thermal aspects all together. As a result, cross-coupling effects among different domains can be taken into account, leading to a more accurate and reliable PMSM design compared to the preliminary analytical one. Furthermore, different optimization criteria have been considered, according to which different PMSMs have been achieved by resorting to a Genetic Algorithm (GA). A performance analysis has been then carried out, whose results reveal the effectiveness of the proposed CDP. Particularly, all the PMSM configurations outperform the preliminary analytical configuration presented in [13], by complying with all electromagnetic, mechanical, and thermal constraints, as well as with all design specifications.

The paper is structured as follows: a brief overview of the ACAES considered in this paper is presented in Section II, together with the definition of PMSM power and speed specifications. Main features and advantages of a modular PMSM configuration are also presented compared to its monolithic counterpart. Section III presents the PMSM multi-physics modeling, based on which the analytical design procedure has been developed (Section IV). The CDP proposed in this paper is then detailed (Section V), whose corresponding results are presented and discussed extensively (Section VI). The manuscript ends with some concluding remarks and future trends (Section VII).

II. SYSTEM OVERVIEW

A schematically representation of the ACAES considered in this paper is shown in Fig. 1, while its main parameters are reported in Table I. The ACAES consists of different compressors (CPs) and turbines (TRs), a Compressed Air Storage (CAS), and several PMSMs connected to the different TMs through clutches and gears. Furthermore, a Thermal Energy Storage (TES) is also concerned, connected to the system through different Heat Exchangers (HEs). Still referring to Fig. 1, the overall system is split into four different pressure stages, namely Low Pressure (LP), Medium Pressure (MP), High Pressure (HP), and Very-High Pressure (VHP) stages, to achieve a very high compression ratio. Each stage includes a CP and a TR, except for the VHP stage that is characterized by a CP only, as resumed in Table II.

ACAES works in two different operating modes, namely charging and discharging. During charging, ACAES is able to store 39 MWh at 6.8 MW, particularly each PMSM absorbs electric power from the electric grid and move the compressors so that the air is compressed and stored into the CAS. When the air comes out from each CP, it is cooled before entering into the following CP, and the heat is stored into the TES. During discharging, ACAES delivers approximately 28 MWh at 9.9 MW; the air from CAS is heated by TES before getting into TRs, in which it expands suitably, generating electric energy through the PMSMs.

This article has been accepted for publication in IEEE Transactions on Industry Applications. This is the author's version which has not been fully edited and content may change prior to final publication. Citation information: DOI 10.1109/TIA.2023.3336312

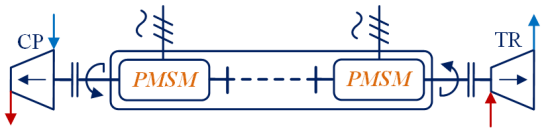

Fig. 2. Modular PMSM configuration.

TABLE III. GEAR RATIOS FOR EACH ACAES TM

TM	TM speed [krpm]	PMSM speed [krpm]	Gear ratio
CP-LP	*12.7*	*12.7*	*1:1*
CP-MP	*21.8*	*14.5*	*1.5:1*
CP-HP	*28.6*	*19*	*1.5:1*
CP-VHP	*29.3*	*19.5*	*1.5:1*
TR-LP	*7.3*	*10.9*	*1:1.5*
TR-MP	*16.7*	*16.7*	*1:1*
TR-HP	*30*	*20*	*1.5:1*

Since ACAES charging and discharging never occur simultaneously, the same PMSM can operate either as a motor (coupled to CP) or as a generator (coupled to TR), with considerable savings in component number and space. Therefore, each PMSM must be designed properly to match the performance required by CP and TR at each stage, as detailed in the following section.

A. *Power and speed specifications*

The definition of the PMSM specifications starts from the power and speed rates of LP, MP, and HP stages, which are made up of a TR and a CP with rated power ranging from 1.7 MW to 3.3 MW, and a rotational speed ranging from 7.3 to 30 krpm (Table II). Differently, the VHP stage consists of a CP only (1.5 MW, 29.3 krpm). Consequently, since the PMSM in each stage must satisfy the performance required during both charging and discharging, a monolithic solution must be characterized by 3.3 MW rated power.

Each PMSM is coupled to the TMs by means of mechanical gears and clutches, which adapt the PMSM speed and torque to those required by each TM. Given the TM speeds reported in Table II, the corresponding PMSM operating speeds have been set as in Table III to achieve a gear ratio not greater than 1.5. Such relatively small values result into very simple transmission systems or even direct drive solutions, thus enabling high power density and efficiency [16]. Consequently, given Table III, the PMSM operating speed range has been set to 10-20 krpm.

Given the high-power and high-speed requirements mentioned above, i.e. 3.3 MW and 10-20 krpm, a monolithic PMSM could not be able to satisfy both, especially due to high mechanical stresses occurring on large rotors at high-speed [13]. In addition, since the PMSM is connected alternatively to TR or CP of the same ACAES stage, which are characterized by different rated powers, the monolithic PMSM operates at rated power only during discharging, whereas it operates at reduced power (approximately 50%) during charging. Consequently, this configuration seems not suitable for the given ACAES, especially because it is oversized for charging, during which the PMSM would work at low efficiency.

Given the limits of the monolithic configuration pointed out previously, a modular cascade PMSM configuration has been considered and proposed in [13] at the aim of achieving both high-power and high-speed operation at each ACAES stage (3.3 MW at LP, MP, and HP, 1.5 MW at VHP, 10-20 krpm for all). This modular configuration consists of several identical PMSM modules with an appropriate rated power and each driven by its own converter, mechanically series-connected to each other in each stage so that they share the same output shaft and speed. More specifically, rated power and speed range of each PMSM module are set at 1.1 MW and 10-20 krpm to achieve four groups of 2-3 identical PMSM modules, as shown in Fig. 2 [13]. In this regard, just 2 PMSM modules are required by the VHP stage, whereas all the other stages need 3 PMSM modules. Consequently, employing the same PMSM module for all the stages reduce designing and manufacturing costs compared to the use of different monolithic PMSMs [14], [15].

The main advantage of this modular configuration is that each module can operate close to its rated power during both ACAES operating modes (charging and discharging), thus guaranteeing enhanced performance and increased efficiency compared to the monolithic configuration. In particular, during discharging, all PMSM modules can operate simultaneously at their rated power, reaching 3.3 MW overall. Differently, during charging, the PMSM modules can be selectively connected to the grid or kept offline, reducing the overall power suitably. Another advantage consists of the lower power required by each module (1.1 MW) compared to its monolithic counterpart (1.5 and 3.3 MW), which results in smaller size and, thus, higher operating speed. Furthermore, in case of failure of one module, the system can still operate at reduced power, avoiding a total shutdown of the ACAES. The modular configuration extends the high-efficiency operating region too, by optimally splitting the torque demand among the modules [17].

Regardless of monolithic or modular configuration, the very high power and speed rates require designing the PMSM through a multi-physics approach that takes into account electromagnetic, mechanical, and thermal aspects simultaneously to match all specifications and constraints, as detailed in the following section.

III. MULTI-PHYSICS MODELING

A. *Electromagnetic modeling and constraints*

From an electromagnetic point of view, the PMSM design must comply mainly with the maximum current density to avoid PM demagnetization and PMSM overheating, as well as with the maximum allowable magnetic flux density in the iron parts to prevent magnetic saturation phenomena. Both these aspects affect the PMSM design significantly, especially its geometry, material choice, operating power and speed range.

Starting from current density (J), it depends on the stator slot area (S_{slot}), the cross section of the copper wire (S_{cu}), and the number of series-connected wires in each slot (N_{cu}), as shown in Fig. 3 and expressed as

$$J = I_n \frac{N_{cu}}{S_{slot} F_s} \tag{1}$$

This article has been accepted for publication in IEEE Transactions on Industry Applications. This is the author's version which has not been fully edited and content may change prior to final publication. Citation information: DOI 10.1109/TIA.2023.3336312

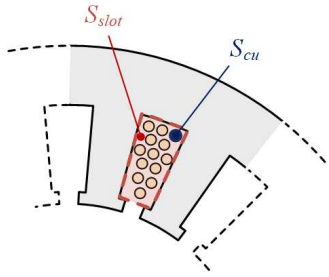

Fig. 3. A detailed view of a PMSM stator slot.

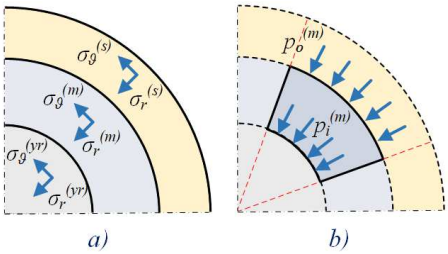

Fig. 4. Rotor cross section with (a) stress and (b) contact pressures highlighted: rotor yoke (grey), PMs (blue), sleeve (yellow).

where I_n is the PMSM rated phase current, and F_s is the slot fill factor:

$$F_s = \frac{S_{cu} N_{cu}}{S_{slot}} . \tag{2}$$

Regardless of the wiring topology, S_{cu} should be chosen suitably small in order to reduce the AC winding losses, including proximity and skin effect losses [18]. However, given a certain current density, if S_{cu} is too small, the current flowing through the wire can be too much high, with a high probability of failure.

Focusing now on the peak magnetic flux density in the rotor and stator iron yoke (B_{yr} and B_{ys}, respectively), these are imposed always lower than the magnetic saturation threshold of the material (B_{max}), leading to the following inequality:

$$B_{yr/ys} \le B_{\max} . \tag{3}$$

These peak values can be obtained by resorting to analytical electromagnetic model or FEA. From an analytical point of view, B_{yr} and B_{ys} can be achieved by considering the magnetic flux density on the contact surface between PMs and the rotor yoke (B_m) [12], [13], which can be expressed as:

$$B_m = \frac{-s_m H_c + n_p \cdot I_n}{f} \tag{4}$$

where n_p is the number of wire turns for phase, whose product with I_n represents the overall stator *mmf*. Moreover, H_c is the PM coercive force, s_m is the PM thickness, while f is

$$f = \frac{r_{yr}}{\mu_m} \ln\left(1 + \frac{s_m}{r_{yr}}\right) + \frac{r_{yr}}{\mu_0} \ln\left(1 + \frac{s_{\delta\_eq}}{r_{yr} + s_m}\right) \tag{5}$$

in which s_{δ_eq} is the equivalent air-gap thicknesses, r_{yr} is the rotor yoke radius, and μ_m is the PM magnetic permeability. Consequently, by assuming radial magnetic flux density, B_{yr} and B_{ys} can be achieved as

$$B_{yr/ys} = \frac{\pi}{2p} \frac{r_{yr}}{s_{yr/ys}} B_m \tag{6}$$

where p is the number of pole pairs, s_{yr} and s_{ys} represent the thickness of the rotor and stator yoke, respectively. It is worth noting that $B_{yr/ys}$ can be reduced by increasing the thickness of rotor/stator yoke, or the number of PMSM pole pairs, e.g. doubling the pole pair numbers means halving $B_{yr/ys}$ [19]. However, as far as high-speed application is concerned, pole pair numbers greater than 2 are usually not recommended because it means high electric frequency and, thus, inverter switching frequency [19]. On the other hand, large stator yoke increases PMSM volume and weight, reducing its power and torque density unsuitably.

A more accurate estimation of $B_{yr/ys}$ than that achievable by (6) can be achieved by FEA. In particular, magnetic field transient analysis allows the computation of the magnetic flux density distribution in the PMSM, taking into account nonlinear phenomena, such as magnetic saturation, PM demagnetization, and temperature variations.

B. Mechanical modeling and constraints

From the mechanical point of view, the rotor design plays a fundamental role as the centrifugal forces due to high-speed operation cause high tensile stress on the rotor, jeopardizing the contact between the PMs and the rotor yoke as well. For these reasons, a retained sleeve, mechanically forced on the PMs, has been considered, which must be carefully designed so that the prestress produced by the interference fit (δ) balances the tensile stress acting on the rotor at high-speed operation [20], [21]. In this regard, the stress contributions in the PMSM rotor parts highlighted in Fig. 4a must be evaluated and compared with the maximum stress allowable by rotor materials, leading to the following constraint:

$$\left|\sigma_x^{(y)}\right| < \left|\frac{\sigma_{x,\max}^{(y)}}{s_f}\right|, \quad x \in \{r, \theta\}, \quad y \in \{yr, m, s\} \tag{7}$$

in which $\sigma_r^{(y)}$ and $\sigma_\theta^{(y)}$ represent the radial and tangential stress acting on the different rotor layer (y), namely the rotor yoke (yr), the PM ring (m), and the sleeve (s), while $\sigma_{x,max}^{(y)}$ represents the maximum allowable stress of the different materials along the direction x. Moreover, s_f is a safety coefficient, which is generally assumed equal or greater than 2 to account for manufacturing uncertainties, inaccuracies, and/or defects [22].

Apart from (7), the contact pressures between the rotor layers shown in Fig. 4b must be always higher than zero to guarantee appropriate adhesion between the different layers at any operating condition, leading to

$$p_{i/o}^{(m)} > 0 \tag{8}$$

in which $p_{i/o}^{(m)}$ represent the internal/external contact pressures acting on the m layer. Both stresses and contact pressures depend on the rotor geometry and material characteristics, and

they can be estimated through the analytical mechanical model, or through FEA. Regarding the analytical approach, an advanced mechanical model has been considered in [13], which takes into account the orthotropic nature of the sleeve made up of epoxy carbon fiber. In this regard, it is worth noting that an isotropic model could be considered in case of thin sleeve, as done in previous works [12], [20], but this cannot be employed further as the thickness of the sleeve increases. Consequently, the analytical expression of σ_r and σ_θ are obtained along the radial direction (r) considering the mechanic-elastic theory applied to a generic rotating pressurized cylinder [20]–[22], resulting in the following relationships:

$$\sigma_r(r) = c_1 r^{k-1} + c_2 r^{-k-1} - \frac{(3+\upsilon_\theta)\rho\omega^2 r^2}{9-k^2} + - E_\theta\left(\frac{r(2\alpha_\theta-\alpha_r)t}{4-k^2} + \frac{(\alpha_\theta-\alpha_r)t_0}{1-k^2}\right) \quad (9)$$

$$\sigma_\theta(r) = kc_1 r^{k-1} - kc_2 r^{-k-1} - \rho\omega^2 r^2\left(\frac{3(3+\upsilon_\theta)}{9-k^2} - 1\right) + - E_\theta\left(\frac{2r(2\alpha_\theta-\alpha_r)t}{4-k^2} + \frac{(\alpha_\theta-\alpha_r)t_0}{1-k^2}\right) \quad (10)$$

where $E_{r/\theta}$, $\upsilon_{r/\theta}$, and $\alpha_{r/\theta}$ are Young's modulus, Poisson's ratio, and thermal expansion coefficients along radial/tangential direction, respectively, while ω is the cylinder rotational speed. Moreover, c_1, c_2, t_0 and t are constant coefficients that depend on the inner and outer cylinder pressures, rotating speed and temperature gradient [21], while k is defined as:

$$k = \sqrt{\frac{E_\theta}{E_r}}\,. \quad (11)$$

The same model can be used when isotropic materials are considered, such as those employed for the PMs. Therefore, the following relationships hold

$$E_\theta = E_r = E \;\;;\;\; \upsilon_\theta = \upsilon_r = \upsilon \;\;;\;\; \alpha_\theta = \alpha_r = \alpha\,. \quad (12)$$

Consequently, (9) and (10) can be rewritten as

$$\sigma_r(r) = c_1 + \frac{c_2}{r^2} - \frac{(3+\upsilon)}{8}\rho\omega^2 r^2 - \frac{E\alpha t}{3} r \quad (13)$$

$$\sigma_\theta(r) = c_1 - \frac{c_2}{r^2} - \rho\omega^2 r^2\left(\frac{3(3+\upsilon)}{8} - 1\right) - \frac{2E\alpha t}{3} r\,. \quad (14)$$

On the other hand, the expression of contact pressures $p_{i/o}^{(m)}$ can be obtained starting from the radial displacement u_r of each rotor layer, which is defined by the Hooke's law as

$$u_r^{(y)} = \frac{r}{E_\theta^{(y)}}\left(\sigma_\theta^{(y)} - k\upsilon_r^{(y)}\sigma_r^{(y)} + E_\theta^{(y)}\alpha_\theta^{(y)}\Delta T^{(y)}\right) \quad (15)$$

in which ΔT is the difference between actual and reference temperature in each rotor layer. Then, the radial deflection associate to the contact pressures on the PM contact surfaces is

$$\left(u_r^{(m)} - u_r^{(yr)}\right)\Big|_{r=r_{sh}+s_{yr}} = 0 \;\;,\;\; \left(u_r^{(s)} - u_r^{(m)}\right)\Big|_{r=r_{sh}+s_{yr}+s_m} = \delta \quad (16)$$

where δ is the mechanical interference fit. Consequently, by substituting (15) in (16) and solving the latter, the parameters c_1 and c_2 can be achieved; these, in turn, enable computing the corresponding contact pressures [21]. Alternatively to analytical approach, more accurate results can be achieved by FEA, particularly mechanical analysis allows the evaluation of $\sigma_r^{(y)}$ and $\sigma_\theta^{(y)}$ in the rotor caused by prestress, rotational speed, and thermal effect.

C. *Thermal modeling and constraints*

From a thermal point of view, overheating phenomena must be avoided in the overall PMSM, but especially in the windings and in the PMs, which represent its critical parts. In particular, high current density values could cause overtemperature in the windings, irreparably damaging the insulation. On the other hand, excessive temperatures can be reached in the PMs due to eddy current losses, which may occur due to the relatively high electrical conductivity of PMs, and/or to an inefficient cooling system. For these reasons, the temperature in the windings (T_{cu}) and in the PMs (T_{PM}) must be kept below the maximum allowed values, leading to

$$T_{cu/PM} < T_{cu,\max/PM,\max}\,. \quad (17)$$

The analytical estimation of the temperature distribution in the PMSM is difficult to achieve, and accurate results are often not obtained. Conversely, temperature estimation in each PMSM part can be achieved more simply and quickly by FEA using a thermal equivalent circuit. This consists of passive components (thermal resistances), which are strictly dependent on machine geometry, materials, cooling system, and case configuration, while heat sources account for copper, core, and eddy current losses. This thermal equivalent circuit enables running a combined magnetic-thermal analysis, which accounts for the variation of some PMSM features due to increases in temperature (coil resistance, PM residual magnetism, etc.), as detailed in Section V.

IV. PMSM ANALTYCAL DESIGN

The PMSM cross-section view is shown in Fig. 5, while its corresponding design specifications are resumed in Table IV. Regarding the PMSM stator, a distributed three-phase winding characterized by 18 slots and 3 slots per pole per phase has been chosen, which guarantees a good sinusoidally-shaped *mmf* created by the stator currents [23]. Furthermore, copper round wires have been considered, guaranteeing a fill factor (F_s) of approximately 40%, and low copper losses at high-speed operation, especially when Litz-wire solutions with small cross-sections are employed [24], [25]. It is worth noting that F_s should be as high as possible to reduce the thermal resistance and the temperature rise. Consequently, rectangular wires, as the hairpin windings, could be employed as they offer higher F_s values, reduced end-winding lengths, and lower low-frequency copper losses than round wires. However, their inherently high ohmic losses at high-frequency operation, where skin and proximity effects occur, curb their spread, especially in high-speed applications [26]. The material employed for the stator core is the typical silicon steel, i.e. M235-35A [27], which

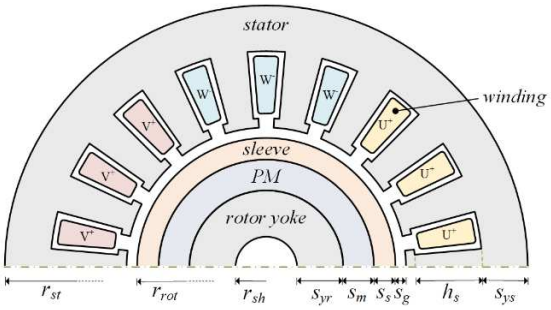

Fig. 5. The PMSM cross-section view.

TABLE IV. PMSM DESIGN SPECIFICATIONS FOR EACH ACAES STAGE

Parameter	Sym	Unit	Analytical	CDP
*Rated power**	P_n	*MW*	*3.3 (1.1)*	-
Rated speed	$\omega_{m,n}$	*krpm*	*10*	
Maximum speed	$\omega_{m,max}$	*krpm*	*20*	
Slot numbers	n_{slot}	-	*18*	
Slot per pole per phase	q	-	*3*	
Winding phase number	m_s	-	*3*	
Slot fill factor	F_s	%	*40*	-
Pole pair numbers	p	-	*1*	
Shaft radius	r_{sh}	*mm*	*40*	
DC-link voltage	V_{DC}	*V*	*3500*	
Convective heat exchange coefficient	h_c	*W/m²/k*	-	*500*
Environment temperature	T_{ext}	*°C*	-	*20*
Fins number	n_{fins}	-	-	*15*

**Monolithic (modular) configuration*

exhibits a maximum flux density value of approximately 1.8 T (B_{max}) and a thickness of the iron plates of 0.35 mm, ensuring very low core losses.

Regarding the PMSM rotor, a configuration with an inner rotor, 2-pole surface-mounted PMs have been considered to enable high-speed operation on condition that an appropriate mechanical sleeve is employed. high-grade NdFeB PMs (N35H [28]) have been selected for their very high energy density, while an epoxy composite carbon fiber (CFRP 60%) has been considered for the sleeve due to its very high mechanical strength. The shaft radius has been set at 40 mm to guarantee a good mechanical match with the TM shaft. In conclusion, the DC-link voltage (V_{DC}) has been set at 3500 V in accordance with common values occurring for the interconnection between transmission and distribution grids, and in medium voltage substations.

Given the design specifications above mentioned, as well as the constraints described in Section III, the PMSM configurations presented in [13] have been obtained through the analytical design procedure shown in Fig. 6. This procedure starts from a multi-parameter array, in which different tunable variables, shown in Table V and representing geometrical quantities, vary independently from each other within appropriate ranges and by appropriate steps. According to PMSM design specifications (Table IV), material properties, and analytical models (Section III), the analytical procedure determines several derived variables, which include geometrical and operating quantities, as summarized in

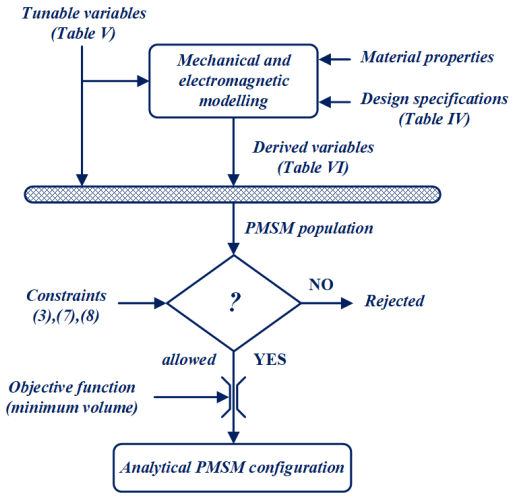

Fig. 6. Flow chart of the PMSM analytical design procedure.

TABLE V. PMSM TUNABLE VARIABLES

Variable	Sym	Unit	Analytical	CDP
Rotor yoke thickness	s_{yr}	*mm*	✓	✓
PM thickness	s_m	*mm*	✓	✓
Sleeve thickness	s_s	*mm*	✓	✓
Axial length	l_i	*mm*	✓	✓
Interference fit	δ	*mm*	✓	✓
Slot height	h_s	*mm*		✓
Stator yoke thickness	s_{ys}	*mm*		✓
Air-gap	s_g	*mm*		✓
Thoot width	s_{th}	*mm*		✓
Current density	J	*A/mm²*		✓
Rated phase current	I_n	*A*		✓
Slot fill factor	F_s	%		✓

Table VI. Tunable and derived variables concur to define a "PMSM population", which is then reduced by rejecting all the PMSM configurations that do not comply with electromagnetic and mechanical constraints (i.e. (3), (7), and (8)). Among all the remaining configurations, the PMSM that satisfies a specific objective function is finally chosen, i.e. that characterized by the minimum volume [13].

A first monolithic PMSM configuration characterized by a rated power of 3.3 MW and a rated torque of 6300 Nm is obtained and presented in [13], whose main parameters are resumed in Table VII. This complies with all constraints and specifications, except for the speed range. In this regard, it has been highlighted in [13] that speed values higher than 10 krpm produce excessive tensile stress on the rotor. Consequently, the speed range specification had to be relaxed down to 5-10 krpm to avoid no solution by the analytical procedure. This relatively low speed range does not address the complexity of the transmission system, requiring gear ratios higher than those imposed in Table III, thus preventing the overall efficiency increase. Hence, this configuration is not suitable for the given ACAES, especially because it is oversized for charging, during which the PMSM would work at low efficiency.

Given the limits of the monolithic PMSM configuration discussed previously, a modular PMSM configuration has been

This article has been accepted for publication in IEEE Transactions on Industry Applications. This is the author's version which has not been fully edited and content may change prior to final publication. Citation information: DOI 10.1109/TIA.2023.3336312

TABLE VI. PMSM DERIVED VARIABLES BY THE ANALYTICAL PROCEDURE

Variable	Sym	Unit
Rated phase current	I_n	*A*
Rated current density	J	A/mm^2
Rated phase voltage	V_n	*V*
Stator yoke thickness	s_{ys}	*mm*
Slot height	h_s	*mm*
Wire turns for slots	n	-
Wire cross section	S_{cu}	mm^2
Magnetic flux density in iron part	$B_{yr/ys}$	*T*
Mechanical stress on the rotor layers	$\sigma_x^{(y)}$	*MPa*
Contact pressures in the PM layer	$p_{i/o}^{(m)}$	*MPa*

TABLE VII. PMSM MAIN PARAMETERS

Parameter	Sym	Unit	Case	
			Monolithic	*Modular*
*Power**	P_n	*kW*	*3300*	*1100*
*Rotational speed**	$\omega_{m,n}$	*krpm*	*5*	*10*
Maximum speed	$\omega_{m,max}$	*krpm*	*10*	*20*
*Torque**	$T_{e,n}$	*Nm*	*6300*	*1050*
*Phase current**	I_n	*A*	*1025*	*527*
*Current density**	J	A/mm^2	*5.6*	*8.6*
*Phase voltage**	V_n	V_{RMS}	*1916*	*1206*
Rotor and stator yoke thickness	$s_{yr/ys}$	*mm*	*100*	*60.0*
PM thickness	s_m	*mm*	*30*	*20.0*
Sleeve thickness	s_s	*mm*	*40*	*30.0*
Air-gap	s_g	*mm*	*3.0*	*3.0*
Slot height	h_s	*mm*	*111*	*49.0*
Stator outer radius	r_{st}	*mm*	*429.0*	*267.0*
Rotor outer radius	r_{rot}	*mm*	*210*	*150.0*
Volume	V	dm^3	*373.0*	*104.0*
Mass	M	*kg*	*2707*	*733*
Radial interference fit	δ	*mm*	*0.3*	*0.5*
Axial length	l_i	*mm*	*650*	*490.0*
Wire cross section	S_{cu}	mm^2	*185.5*	*61.2*
Slot area	S_{slot}	mm^2	*1855*	*1223*
Slot fill factor	F_s	*%*	*40.0*	*40.0*
Wire turns for slots	n	-	*4*	*8*

**At rated condition* (T_n,$\omega_{m,n}$)

considered and still proposed in [13] at the aim of increasing maximum speed and flexibility. Differently from the monolithic configuration, the modular one is able to comply with all design specifications and constraints, as highlighted in Table VII

V. PMSM COMBINED DESIGN PROCEDURE

The analytical procedure presented in [13] and resumed previously can be carried out in a very short time, simplifying the designer's efforts considerably. However, the procedure first requires modeling each physical phenomenon under consideration analytically, which is usually far from trivial. Second, the procedure does not take into account the coupling effects among different domains, such as the electromagnetic performance variations due to temperature increase. Third, when a high number of tunable variables or a very short variation step is considered, the computation time of the analytical procedure increases considerably, which may also

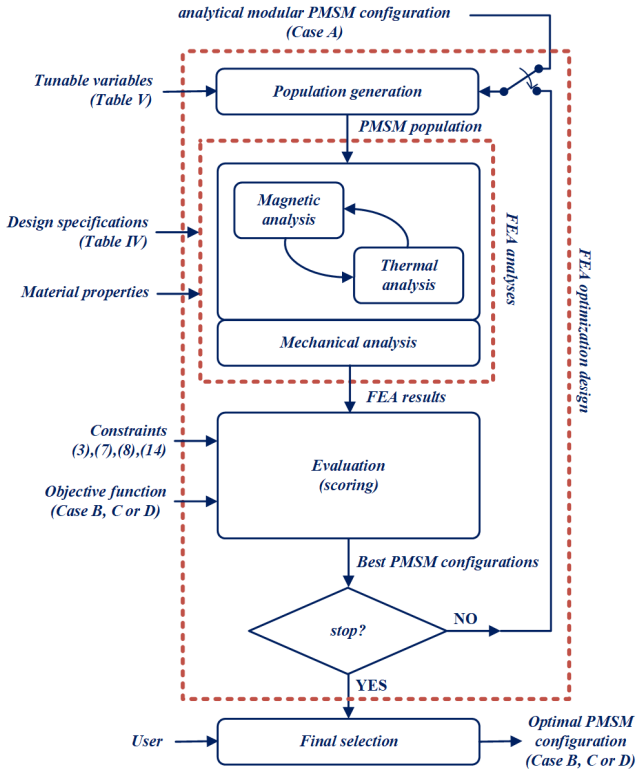

Fig. 7. Flow chart of the FEA approach making the proposed CDP.

lead to out-of-memory issues.

All these drawbacks can be overcome by resorting to the multi-physics CDP proposed in this paper, which relies on a preliminary analytical design to refine it by FEA and a Genetic Algorithm (GA) embedded into the FEA software. Starting from the PMSM modular configuration obtained in [13], whose main parameters are reported in Table VII and repeated in Table VIII (case A), the GA generates the first PMSM population by varying the tunable variables within their operating ranges, as in Fig. 7. In this regard, many more tunable variables than the analytical approach are considered, also including operating parameters, as reported in Table V. Subsequently, PMSM population undergoes a combined transient magnetic-thermal analysis, followed by a mechanical analysis, which strictly depend on design specifications (Table IV) and material properties, as shown in Fig. 7. More specifically, magnetic and thermal analyses are run alternately at each simulation step and iteratively, namely magnetic analysis benefits from the updated temperature obtained by the thermal circuit, while updating heat sources employed by the latter. This combined analysis results in better estimating PMSM electromagnetic performance compared to the analytical procedure, in which temperature variation is not considered due to the complexity of the subsequent analytical modeling.

Regarding thermal design specifications (Table IV), an external case configuration with 15 fins is considered in order to facilitate the heat exchange with the external environment, whose temperature is assumed equal to 20 °C. Furthermore, a forced air-cooling system in the air-gap axial direction has been taken into account to enhance heat dissipation, guaranteeing a

This article has been accepted for publication in IEEE Transactions on Industry Applications. This is the author's version which has not been fully edited and content may change prior to final publication. Citation information: DOI 10.1109/TIA.2023.3336312

TABLE VIII. PMSM DESIGN OPTIMIZATION RESULTS

Parameter	Sym	Unit	Case			
			A	B	C	D
Power*	P_n	kW	1100	1090	1097	1101
Rotational speed*	$\omega_{m,n}$	krpm	10	10	10	10
Maximum speed	$\omega_{m,max}$	krpm	20	20	20	20
Torque*	$T_{e,n}$	Nm	1050	1041	1047	1051
Phase current*	I_n	A	527	517	375	520
Current density*	J	A/mm^2	8.6	5.8	5.3	6.3
Phase voltage*	V_n	V_{RMS}	1206	1213	1596	1277
Rotor yoke thickness	s_{yr}	mm	60.0	45.7	45.7	45.7
Stator yoke thickness	s_{ys}	mm	60.0	60.0	58.0	45.3
PM thickness	s_m	mm	20.0	20.0	20.0	20.0
Sleeve thickness	s_s	mm	30.0	14.1	14.1	19.9
Air-gap	s_g	mm	3.0	2.0	2.0	1.8
Slot height	h_s	mm	49.0	44.4	61.2	44.0
Thoot width	s_{th}	mm	35.0	11.4	30.0	11.4
Stator outer radius	r_{st}	mm	267.0	229.2	244.0	219.8
Rotor outer radius	r_{rot}	mm	150.0	119.8	119.8	126.6
Volume	V	dm^3	104.0	70.8	94.0	66.0
Mass	M	kg	733	539	710	494
Radial interference fit	δ	mm	0.5	0.4	0.4	0.4
Axial length	l_i	mm	490.0	405.8	500.0	405.8
Wire cross section	S_{cu}	mm^2	61.2	88.2	70.8	82.5
Slot area	S_{slot}	mm^2	1223	1773	1479	1872
Slot fill factor	F_s	%	40.0	44.8	43.1	44.0
Wire turns for slots	n	-	8	9	9	10

*At rated condition (T_n,$\omega_{m,n}$)

convective heat exchange coefficient of 500 W/m^2/K [29]. All these features concur to ensure the compliance with the temperature limits in the winding and in the PMs, which are 250 °C and 90 °C, respectively [28]. On the other hand, the mechanical analysis is carried out in cascade to the magnetic-thermal analysis and allows the evaluation of the mechanical stress on the rotor.

Once FEA results have been achieved, PMSM population is scored accordingly, by considering all constraints and a given objective function. In this regard, three different objective functions have been set and employed alternatively, which consist of the minimization of torque ripple (case B), the maximization of the efficiency (case C), and the maximization of the torque density (case D). The best PMSM configurations of the current generation are thus obtained and, if the GA stopping criterion is not met, a new generation of PMSM population is setup accordingly, and the procedure is repeated iteratively. When the stopping criterion is satisfied, which is, in this case, the maximum number of generations, the user selects the optimal PMSM configuration manually among the best PMSM configurations belonging to the last generation.

In conclusion, it is worth noting that the maximum number of generations, as well as the population size for each generation and the number of best PMSM configurations, should be selected to guarantee GA convergence. In this paper, these have been set to 50, 100, and 10, respectively.

A. *Optimization results*

The main features of the PMSM optimized configurations obtained by the CDP are summarized in Table VIII, together with those of the original modular configuration already presented in [13] (case A). In particular, these configurations achieve minimum torque ripple (case B), maximum efficiency (case C), and maximum torque density (case D). Table VIII reveals that all PMSM configurations achieved by the CDP are characterized by a lower volume than case A, which should not have occurred as the latter was achieved by minimizing PMSM volume through the analytical procedure. Such an unexpected outcome is due to the increased number of tunable variables employed by the CDP, e.g. tooth width, current density and slot fill factor, which are set constant in [13], thus preventing a proper volume optimization. The increased effectiveness of the CDP is due also to taking into account the cross-coupling effects among different domains. In addition, the knowledge of the main parameters of Case A obtained in [13] allows the setting of the tunable variables employed for the CDP. This guarantees a narrow range for each tunable variable, which helps the GA to avoid geometrical conflicts. Consequently, the analytical procedure proposed in [13] does not lose its usefulness as it is preparatory for the optimized FEA procedure and, thus, part and parcel of the proposed CDP, making the latter innovative compared to many other design procedures presented in the literature.

VI. FEA RESULTS

A. *Electromagnetic results*

The FEA results related to all the modular PMSM configurations considered in this paper (cases A-D) are shown from Fig. 8 to Fig. 12, and resumed in Table IX. The first optimized configuration (case B) exhibits the minimum torque ripple (2.06 %), with a reduction of 62.7 % compared to case A, as pointed out in Table IX. This is also shown in Fig. 8, which reports the torque evolution at rated operating conditions for all cases. Case B is also characterized by a lower volume than case A, which results in a good increase in torque density (14.7 kNm/m^3 vs 10 kNm/m^3), and by a higher slot area (Table VIII), leading to a lower current density and, consequently, lower Joule losses (Table IX). In addition, case B exhibits higher values of magnetic flux density in the stator, as shown in Fig. 9; this is still far from the magnetic saturation threshold, meaning a core exploitation better than case A. However, this also means higher core losses (Table IX) and stator core loss density (Fig. 10), especially in the stator teeth. It is worth noting that the core losses increase achieved in case B is much more than compensated by Joule losses decrease compared to case A, as proved by Table IX and by the overall loss maps depicted in Fig. 11. The latter reveals that case B presents lower overall losses than case A at any operating condition, which results in higher efficiency, especially at high speed operation (Fig. 12).

Regarding case C, the maximum efficiency is achieved by reducing Joule losses significantly compared to cases A and B, as highlighted in Table IX. Consequently, despite increased core losses, the overall losses achieved in case C are the lowest,

This article has been accepted for publication in IEEE Transactions on Industry Applications. This is the author's version which has not been fully edited and content may change prior to final publication. Citation information: DOI 10.1109/TIA.2023.3336312

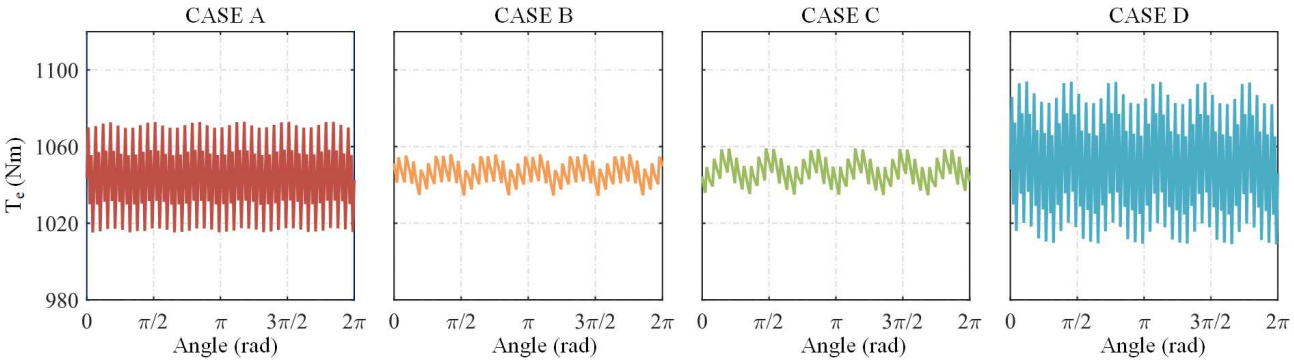

Fig. 8. Torque evolution at rated operating condition for all the designed PMSMs.

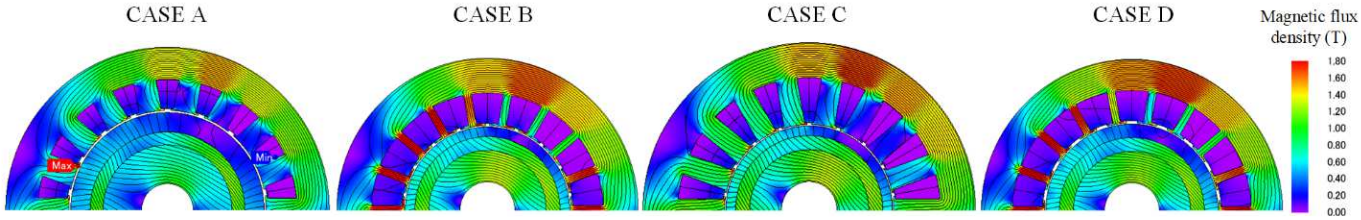

Fig. 9. Magnetic flux density distribution at rated operating conditions for all the designed PMSMs.

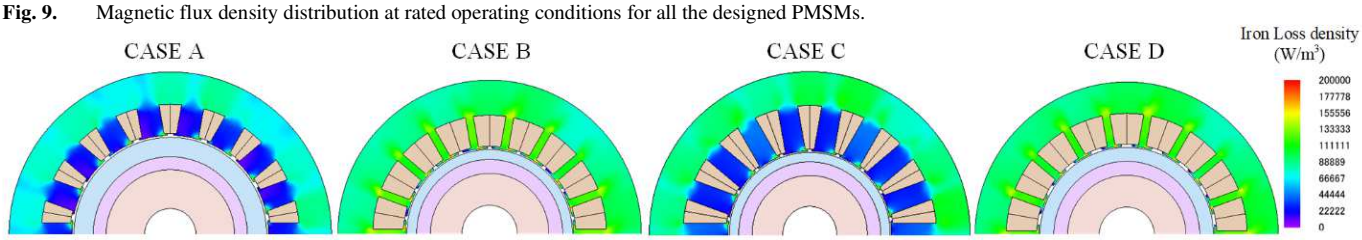

Fig. 10. Stator core loss density distribution at rated operating conditions for all the designed PMSMs.

and the efficiency is the highest, as highlighted in Fig. 11 and Fig. 12, respectively. These features are justified by lower current values and, consequently, lower current density compared to cases A and B (Table VIII). Case C exhibits stator radial dimensions similar to case A, but smaller rotor radius. Therefore, although the axial length is slightly greater than case A, the overall volume is smaller, but greater than case B. As a result, torque density is lower than case B (11.1 kNm/m^3 vs 14.7 kNm/m^3, Table IX), while torque ripple is quite similar (2.34% vs 2.06%, Table IX and Fig. 8).

The third configuration (case D) maximizes the torque density, exhibiting the lowest volume (approximately 63% of case A) and radial dimensions, as well as the highest rated torque among all cases (Table VIII). This results in the highest torque density (15.9 kNm/m^3, Table IX), with an improvement of approximately 59% compared to case A. However, case D is characterized by the highest torque ripple (8.08%, Table IX and Fig. 8), which produces undesired noise and vibrations [30]. Additionally, losses and efficiency are more similar to case A than to cases B and C (Table IX, Fig. 11, and Fig. 12), although Fig. 12 reveals efficiency values at high-speed operation higher than all the other cases.

B. Thermal results

From a thermal point of view, Fig. 13 and Table IX show the temperatures reached at steady-state operation in the different PMSM parts, by employing a similar external case and the same cooling system for each case. In particular, the external case thickness (h_c) has been set at 10 mm, and it is equipped with 15 fins, each of which presents a thickness of 5 mm and a height (h_f) of 50 mm. The temperature in the windings and in the PMs both comply with maximum values of the selected materials, i.e. 250 and 90 °C, respectively. The maximum temperature in the windings is achieved in case D (202.8 °C), while case C exhibits the highest PM temperature (83.3 °C). The former temperature is justified by the lowest PMSM total volume that makes heat exchange more difficult than in other cases. The latter temperature is instead due to the highest PM volume, which results in the highest eddy current losses.

C. Mechanical results

The mechanical stresses acting on the rotor sleeve at $\omega_{m,max}$ for all cases are shown in Fig. 14 and Fig. 15. In particular, Fig. 14 highlights that the maximum tangential stress is widely below the limit threshold (1400 MPa) in all cases, with a maximum value of 570 MPa. Similarly, Fig. 15 highlights that the maximum absolute value of the radial stress is approximately 100 MPa, in line with the corresponding limit threshold (100 MPa). Consequently, rotor integrity is always guaranteed in any case and at any operating condition, as well as torque transmission. This last feature is confirmed by Fig. 16, which highlights the distribution of the radial stress on the PMs. Particularly, the negative values achieved on the inner and outer PM surfaces represent the opposite of the inner and outer

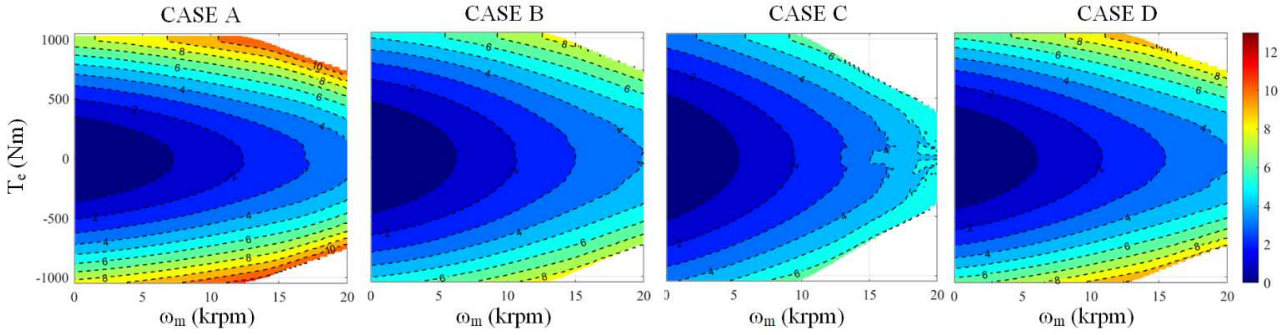

Fig. 11. Overall loss map (Iron losses + Joule losses) in kW for all the designed PMSMs.

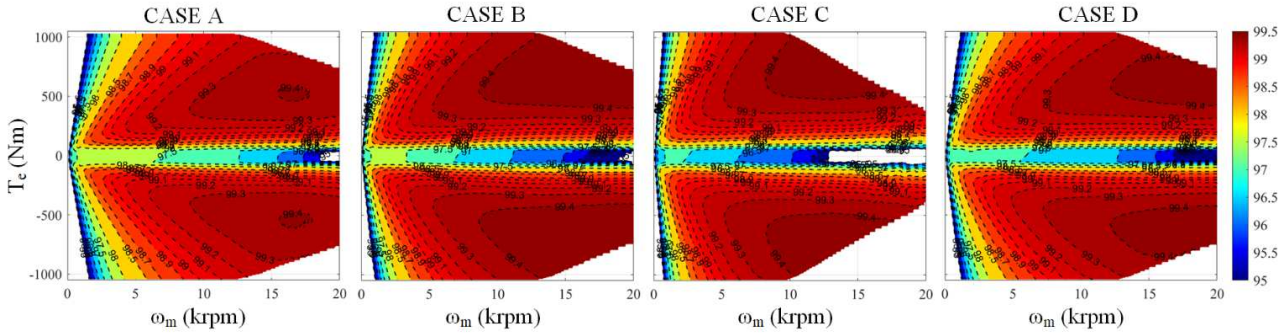

Fig. 12. Efficiency map for all the designed PMSMs

TABLE IX. FEA MAIN RESULTS

Parameter	Sym	Unit	Case			
			A	*B*	*C*	*D*
Electromagnetic						
*Iron loss**	P_i	*W*	*2399*	*2618*	*3521*	*3172*
*Joule loss**	P_j	*W*	*8462*	*5521*	*3873*	*6780*
*Efficiency**	η	*%*	*99.0*	*99.2*	***99.4***	*99.1*
*Torque ripple**	T_{ripple}	*%*	*5.53*	***2.06***	*2.34*	*8.08*
*Torque density**	T_{dens}	*kNm/m³*	*10.0*	*14.7*	*11.1*	***15.9***
*Stator max flux density**	B_{ys}	*T*	*1.50*	*1.64*	*1.69*	*1.71*
*Rotor max flux density**	B_{yr}	*T*	*0.81*	*1.28*	*1.28*	*1.18*
Thermal						
*PM max temperature**	T_{PM}	*°C*	*50.8*	*67.3*	*83.3*	*78.0*
*Wire max temperature**	T_{Cu}	*°C*	*165.2*	*170.9*	*133.1*	*202.8*
Mechanical						
*Sleeve tangential stress***	$\sigma_\theta^{(s)}$	*MPa*	*594*	*554*	*554*	*544*
*Sleeve radial stress***	$\sigma_r^{(s)}$	*MPa*	*-98*	*-61*	*-61*	*-76*
*PM contact pressure***	$p_i^{(m)}$	*MPa*	*44*	*10*	*10*	*28*

**At rated condition (T_n,$\omega_{m,n}$), **At maximum speed ($\omega_{m,max}$)*

contact pressures acting on the PMs. Therefore, these contact pressures are always higher than zero, as also summarized in Table IX, thus complying with mechanical constraints.

In conclusion, the comparison among all the considered configurations is further resumed in the parallel axes plot shown in Fig. 17. The comparative analysis reveals that all the three PMSMs obtained by FEA optimization present geometric dimensions and weight lower than case A, especially cases B and D. Overall performance are also improved compared to case A, which presents just a torque ripple lower than case D, proving the effectiveness of the proposed CDP.

VII. CONCLUSION

A multi-physics Combined Design Procedure (CDP) applied to a high-power/high-speed Permanent Magnet Synchronous Machines (PMSM) for an Adiabatic Compressed Air Energy Storage system (ACAES) has been presented in this paper. The designed PMSMs are intended to be part of a modular system made up of a number of identical modules, mechanically connected to each other and to each ACAES stage (compressor and turbine alternatively). Particularly, modular PMSM configuration benefits from higher speed range, reduced size, improved efficiency and flexibility compared to monolithic solutions, by reducing designing, manufacturing, and maintenance costs as well.

Starting from a preliminary modular PMSM configuration, which has been achieved by an analytical design procedure, the proposed CDP combines the analytical procedure with a Finite Element Analysis (FEA) optimization, which has been carried out through a genetic algorithm by employing different objective functions. The comparison between the optimal PMSM configurations achieved by the proposed CDP and the analytical configuration reveals an overall performance increase due to a more accurate and flexible design. This is achieved by employing the relatively simple and fast analytical procedure to achieve a preliminary PMSM configuration, further refining it by FEA optimization in accordance with the desired optimization target (minimum volume, maximum efficiency, etc.).

Given all the benefits above mentioned, the proposed CDP presents also some limitations. Among these, the number of tunable variables cannot be increased excessively because this would lead to unfeasible computation time and/or out-of

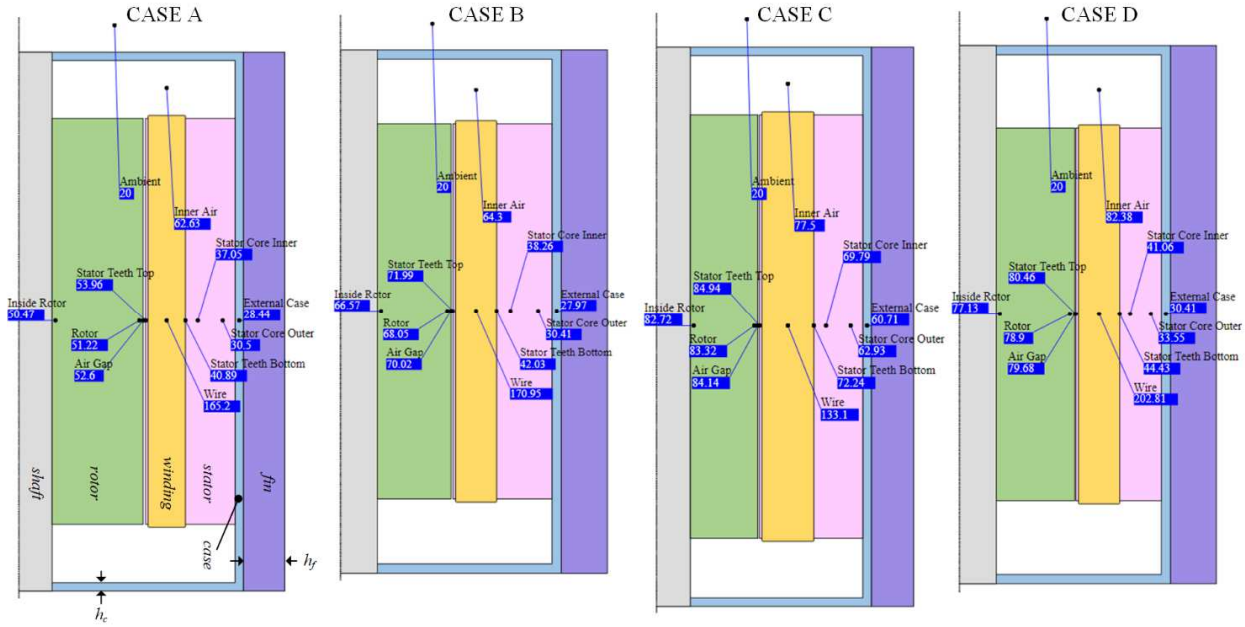

Fig. 13. Axial view of the designed PMSM modules, including external case and fins, as well as the temperature in each part.

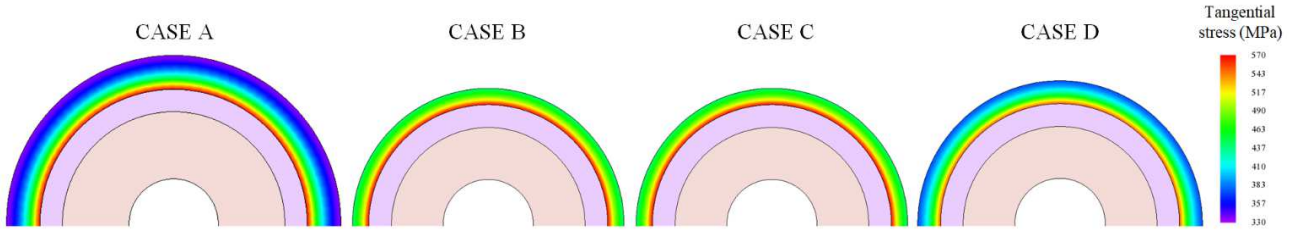

Fig. 14. Sleeve tangential stress distribution at maximum speed (20 krpm) for all the designed PMSMs.

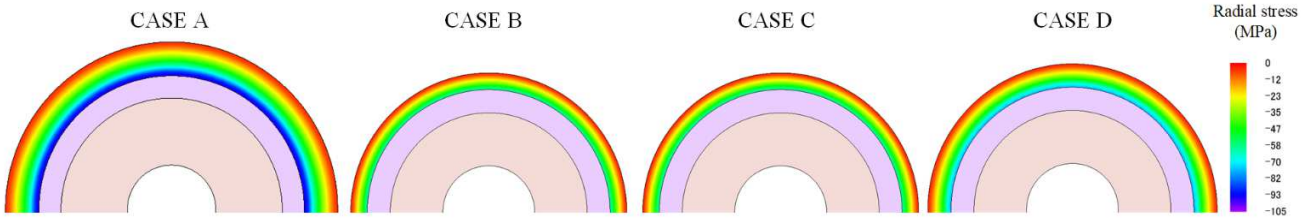

Fig. 15. Sleeve radial stress distribution at maximum speed (20 krpm) for all the designed PMSMs.

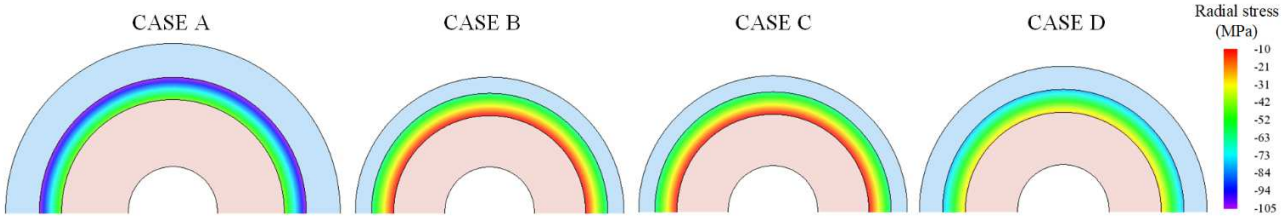

Fig. 16. PM radial stress distribution at maximum speed (20 krpm) for all the designed PMSMs.

memory issues. Furthermore, optimization should be achieved not at a specific operating condition but within a suitable operating range, as generally required by other applications (e.g. electric vehicles). Final selection of the optimal PMSM configuration by the user should be avoided as well.

In the light of such limitations, other optimization algorithms and/or FEA software could be employed, as well as increasing tunable variables at the cost of expensive platforms (e.g. workstations) or by reducing FEA accuracy. Further improvements should also regard control system design and real-time co-simulations to test and further optimize the proposed configurations, also at dynamic operation and at different operating conditions.

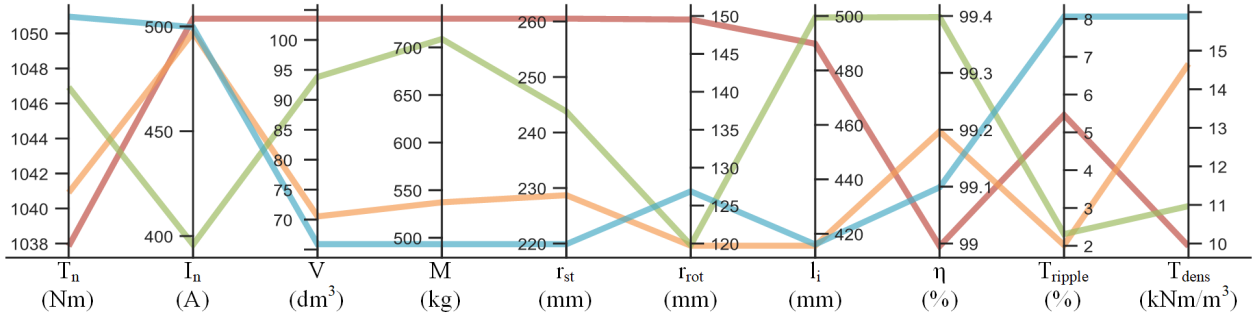

Fig. 17. Parallel axes plot of the designed PMSMs: Case A (red), Case B (orange), Case C (green), and Case D (blue).

VIII. REFERENCES

[1] N. Hatziargyriou, H. Asano, R. Iravani, and C. Marnay, "Microgrids," *IEEE Power Energy Mag.*, vol. 5, no. 4, pp. 78–94, Jul. 2007, doi: 10.1109/MPAE.2007.376583.

[2] F. Katiraei, R. Iravani, N. Hatziargyriou, and A. Dimeas, "Microgrids management," *IEEE Power Energy Mag.*, vol. 6, no. 3, pp. 54–65, May 2008, doi: 10.1109/MPE.2008.918702.

[3] V. A. Boicea, "Energy Storage Technologies: The Past and the Present," *Proc. IEEE*, vol. 102, no. 11, pp. 1777–1794, Nov. 2014, doi: 10.1109/JPROC.2014.2359545.

[4] I. Calero, C. A. Cañizares, and K. Bhattacharya, "Compressed Air Energy Storage System Modeling for Power System Studies," *IEEE Trans. Power Syst.*, vol. 34, no. 5, pp. 3359–3371, Sep. 2019, doi: 10.1109/TPWRS.2019.2901705.

[5] P. Perazzelli and G. Anagnostou, "Design issues for compressed air energy storage in sealed underground cavities," *J. Rock Mech. Geotech. Eng.*, vol. 8, no. 3, pp. 314–328, Jun. 2016, doi: 10.1016/j.jrmge.2015.09.006.

[6] G. Grazzini and A. Milazzo, "A Thermodynamic Analysis of Multistage Adiabatic CAES," *Proc. IEEE*, vol. 100, no. 2, pp. 461–472, Feb. 2012, doi: 10.1109/JPROC.2011.2163049.

[7] Z. Zhang, M. Wang, T. Zheng, N. Zhang, Y. Zhang, and S. Mei, "Performance Analysis of Advanced Adiabatic Compressed Air Energy Storage System with Constant-volume and Adiabatic Gas storage Model under Multi-cycle Operation," in *2020 IEEE Sustainable Power and Energy Conference (iSPEC)*, Nov. 2020, pp. 1425–1430. doi: 10.1109/iSPEC50848.2020.9351278.

[8] A. Chaaran, R. Narendhar, and D. Karthikeyan, "Advanced Adiabatic Compressed air Energy Storage Energy in Air," in *2018 4th International Conference on Electrical Energy Systems (ICEES)*, Feb. 2018, pp. 737–741. doi: 10.1109/ICEES.2018.8442374.

[9] F. T. Jorgensen, "Design and construction of permanent magnetic gears," Institute of Energy Technology, Aalborg University, Aalborg, 2010.

[10] R. R. Moghaddam, "High speed operation of electrical machines, a review on technology, benefits and challenges," in *Proc. of IEEE Energy Conversion Congress and Exposition (ECCE 2014)*, Pittsburgh (USA), Sep. 2014, pp. 5539–5546. doi: 10.1109/ECCE.2014.6954160.

[11] D. Calabrese, G. Tricarico, E. Brescia, G. L. Cascella, V. G. Monopoli, and F. Cupertino, "Variable Structure Control of a Small Ducted Wind Turbine in the Whole Wind Speed Range Using a Luenberger Observer," *Energies*, vol. 13, no. 18, Art. no. 18, Jan. 2020, doi: 10.3390/en13184647.

[12] A. Damiano, A. Floris, G. Fois, I. Marongiu, M. Porru, and A. Serpi, "Design of a High-Speed Ferrite-Based Brushless DC Machine for Electric Vehicles," *IEEE Trans. Ind. Appl.*, vol. 53, no. 5, pp. 4279–4287, Sep. 2017.

[13] A. Floris, A. Damiano, and A. Serpi, "Design of High-Speed/High-Power PM Synchronous Machines for an Adiabatic Compressed Air Storage System," in *2022 International Conference on Electrical Machines (ICEM)*, Sep. 2022, pp. 935–941. doi: 10.1109/ICEM51905.2022.9910751.

[14] S. Cui, S. Han, and C. C. Chan, "Overview of multi-machine drive systems for electric and hybrid electric vehicles," in *2014 IEEE Conference and Expo Transportation Electrification Asia-Pacific (ITEC Asia-Pacific)*, Aug. 2014, pp. 1–6. doi: 10.1109/ITEC-AP.2014.6940988.

[15] S. Han, S. Cui, X. Zhang, H. Ge, and B. Xu, "The Modular Cascade Machines in electric vehicles," in *2012 IEEE Vehicle Power and Propulsion Conference*, Oct. 2012, pp. 1–6. doi: 10.1109/VPPC.2012.6422660.

[16] D. Fodorean, "State of the Art of Magnetic Gears, their Design, and Characteristics with Respect to EV Application," in *Modeling and Simulation for Electric Vehicle Applications*, M. A. Fakhfakh, Ed., InTechOpen, 2016. doi: 10.5772/64174.

[17] S. Han, K. Li, S. Cui, C. Zhu, and W. Zheng, "Torque distribution strategy for modular cascade machines used in EVs," *IEEJ Trans. Electr. Electron. Eng.*, vol. 14, Mar. 2019, doi: 10.1002/tee.22883.

[18] F. Magnussen and C. Sadarangani, "Winding factors and Joule losses of permanent magnet machines with concentrated windings," in *IEEE International Electric Machines and Drives Conference, 2003. IEMDC'03.*, Jun. 2003, pp. 333–339 vol.1.

[19] J. R. Hendershot and T. J. E. Miller, *Design of brushless permanent-magnet machines*. Venice, Florida: Motor Design Books, 2010.

[20] A. Damiano, A. Floris, G. Fois, M. Porru, and A. Serpi, "Modeling and Design of PM Retention Sleeves for High-Speed PM Synchronous Machines," in *Proc. of 6th International Electric Drives Production Conference (EDPC 2016)*, Nuremberg (Germany), Dec. 2016.

[21] A. Floris, M. Paderi, A. Damiano, F. Aymerich, and A. Serpi, "Design criteria and methodology of a Multi-Rim Carbon-fibre Flywheel to be integrated within a Large-Airgap PMSM," in *IECON 2020 The 46th Annual Conference of the IEEE Industrial Electronics Society*, Oct. 2020, pp. 913–919. doi: 10.1109/IECON43393.2020.9255025.

[22] R. G. Budynas, *Advanced Strength and Applied Stress Analysis*, 2nd Edition. Boston: McGraw-Hill Higher Education, 1998.

[23] J. Pyrhonen, T. Jokinen, and V. Hrabovcova, *Design of Rotating Electrical Machines*, 2 edizione. John Wiley & Sons Inc, 2013.

[24] A. Bardalai, X. Zhang, T. Zou, D. Gerada, J. Li, and C. Gerada, "Comparative Analysis of AC losses with round magnet wire and Litz wire winding of a High – Speed PM Machine," in *2019 22nd International Conference on Electrical Machines and Systems (ICEMS)*, Aug. 2019, pp. 1–5. doi: 10.1109/ICEMS.2019.8922173.

[25] S. Li, Y. Li, W. Choi, and B. Sarlioglu, "High-Speed Electric Machines: Challenges and Design Considerations," *IEEE Trans. Transp. Electrification*, vol. 2, no. 1, pp. 2–13, Mar. 2016, doi: 10.1109/TTE.2016.2523879.

[26] E. Preci *et al.*, "Segmented Hairpin Topology for Reduced Losses at High-Frequency Operations," *IEEE Trans. Transp. Electrification*, vol. 8, no. 1, pp. 688–698, Mar. 2022, doi: 10.1109/TTE.2021.3103821.

[27] "m235-35a.pdf." Accessed: Jan. 31, 2023. [Online]. Available: https://www.tatasteeleurope.com/sites/default/files/m235-35a.pdf

[28] "Sintered-Neodymium-Iron-Boron-NdFeB-Magnets-Specifications.pdf." Accessed: Jan. 31, 2023. [Online]. Available: https://www.advancedmagnets.com/wp-content/uploads/2020/07/Sintered-Neodymium-Iron-Boron-NdFeB-Magnets-Specifications.pdf

[29] Y. A. Cengel, *Heat Transfer: A Practical Approach*, 2nd ed. Boston: McGraw Hill Higher Education, 2002.

[30] E. Brescia, M. Palmieri, G. L. Cascella, and F. Cupertino, "Optimal Tooth Tips Design for Cogging Torque Suppression of Permanent Magnet Machines with a Segmented Stator Core," in *2020 International Conference on Electrical Machines (ICEM)*, Aug. 2020, pp. 1930–1936. doi: 10.1109/ICEM49940.2020.9270968.

This article has been accepted for publication in IEEE Transactions on Industry Applications. This is the author's version which has not been fully edited and content may change prior to final publication. Citation information: DOI 10.1109/TIA.2023.3336312

IX. BIOGRAPHY

Andrea Floris (Member, IEEE) received the bachelor's degree in mechanical engineering, and the master's degree in energy engineering from the University of Cagliari, Italy, in 2012 and 2015, respectively. In 2020 he received the Ph.D degree in electronic and computer engineering at the same university. Dr. Floris is currently Assistant Professor at the Department of Electrical and Electronic Engineering of the same university. He is co-author of 16 papers published in international conference proceedings and journals. His research activity regards the design of high-speed electrical machines, flywheel energy storage systems and magnetic gear transmission systems for electric vehicles. He received an IEEE Best Poster Presentation Award.

Alfonso Damiano (Senior Member, IEEE) received the master's degree in electrical engineering from the University of Cagliari, Italy, in 1992. In 1994, he joined the Department of Electrical and Electronic Engineering of the same university as an Assistant Professor, where he became Associate Professor (from 2001 to 2018) and, then Full Professor (since 2018) of electrical machines and energy management. He has co-authored more than 170 papers published in international conference proceedings and journals. His current research interests include multiphase and high-speed electrical machines and drives, management and control of electric vehicles, and energy storage systems. Prof. Damiano is a reviewer for several international conferences and journals. He received an IEEE Paper Award.

Alessandro Serpi (Member, IEEE) received the master's degree in electrical engineering and the Ph.D. in industrial engineering at the University of Cagliari, Italy, in 2004 and 2009, respectively. From 2016 to 2021 he was Assistant Professor at the Department of Electrical and Electronic Engineering of the same university, where he is now Associate Professor. Prof. Serpi is also co-founder, Chief Executive and Technology Officer of NEPSY srl, an academic spin-off company dealing with novel and highly integrated electric propulsion systems. He is co-author of approximately 100 papers published in international conference proceedings and journals. His research activity focuses on management, design and control of electrical machines, drives and energy storage systems. Prof. Serpi is a reviewer for several international conferences and journals. He received three IEEE award